Day 2: Experimental approaches for nonlinear energy harvesting

Sondipon Adhikari, FRAeS

Zienkiewicz Centre for Computational Engineering, College of Engineering, Swansea University, Bay Campus, Swansea, Wales, UK, Email: S.Adhikari@swansea.ac.uk
Twitter: @ProfAdhikari, Web: http://engweb.swan.ac.uk/~adhikaris

SPARC Course: Metamaterial and metasandwich for energy harvesting and vibration control

March 27, 2021

Outline of this talk

Swansea University
Prifysgol Abertawe

Nonlinear energy harvester

- The harvesting of ambient vibration energy for use in powering low energy electronic devices has formed the focus of much recent research.
- Of the published results that focus on the piezoelectric effect as the transduction method, most have focused on harvesting using cantilever beams and on single frequency ambient energy, i.e., resonance based energy harvesting.
- Several authors have proposed methods to optimise the parameters of the system to maximise the harvested energy.
- Some authors have considered energy harvesting under wide band excitation.
- A key challenge is to broadening the frequency band-width over which energy can be harvested efficiently.
- Nonlinear energy harvesters are proposed specifically to address this issue.

Types of nonlinear energy harvester

- Unlike a linear energy harvester, which essentially as the same design, nonlinear energy harvesters can come in various forms. Indeed many concepts have been proposed.
- The key distinguishable feature of a nonlinear energy harvester is that can be multiple stable points in their dynamics.
- This effectively makes them a collection of different linearised harvesters at different excitation regimes within one physical device.
- It is this fact which makes them attractive from a practical stand point.
- However, this advantage comes with many challenges such as difficulties in understanding, analysing, computing, simulating and manufacturing nonlinear energy harvesters.
- We will study a particular system in details to gain fundamental insights into nonlinear energy harvesters.

Piezomagnetoelastic energy hrvestor

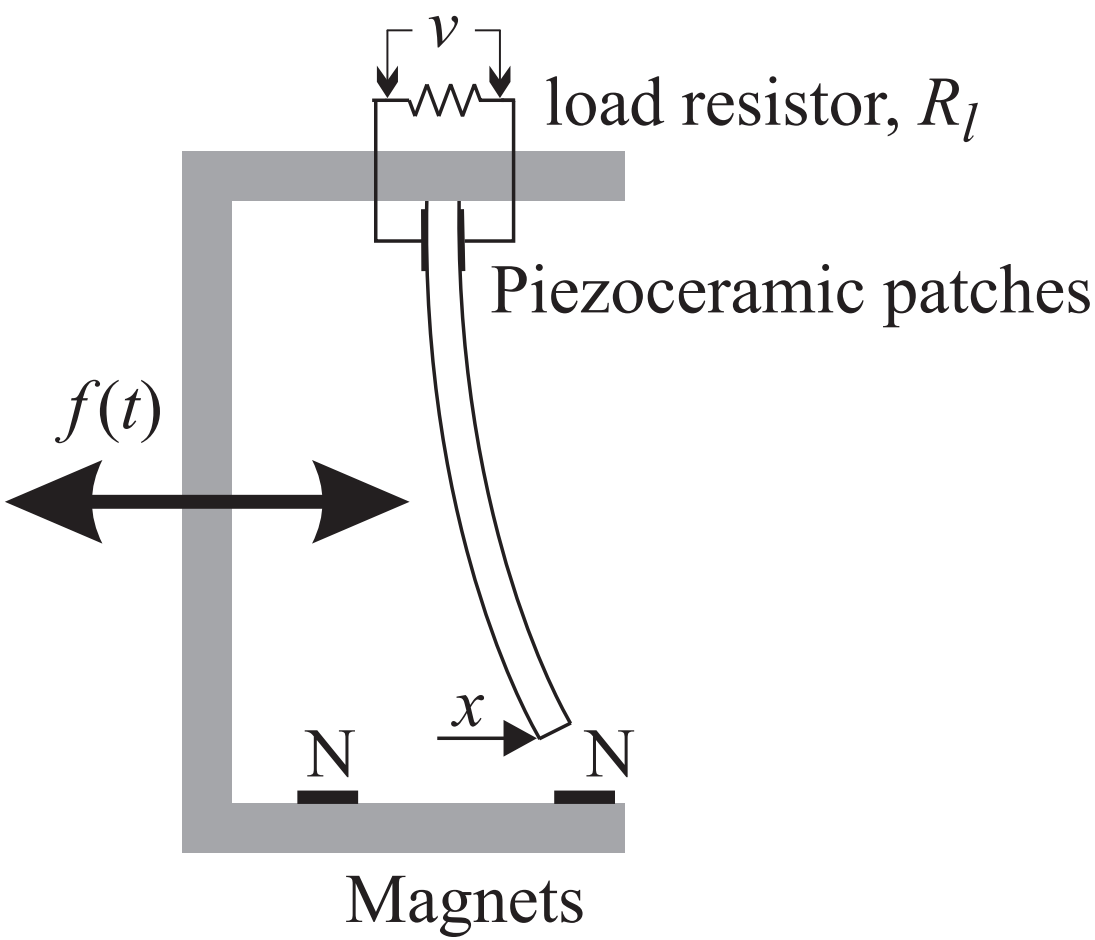

Schematic of the piezomagnetoelastic device. The beam system is also referred to as the 'Moon Beam'.

Governing equations

- The nondimensional equations of motion for this system are

$$\ddot{x} + 2\zeta\dot{x} - \frac{1}{2}x(1 - x^2) - \chi v = f(t), \tag{1}$$

$$\dot{v} + \lambda v + \kappa\dot{x} = 0, \tag{2}$$

- Here x is the dimensionless transverse displacement of the beam tip, v is the dimensionless voltage across the load resistor, χ is the dimensionless piezoelectric coupling term in the mechanical equation, κ is the dimensionless piezoelectric coupling term in the electrical equation, $\lambda \propto 1/R_l C_p$ is the reciprocal of the dimensionless time constant of the electrical circuit, R_l is the load resistance, and C_p is the capacitance of the piezoelectric material.
- The force $f(t)$ is proportional to the base acceleration on the device.
- If we consider the inductor, then the second equation will be $\ddot{v} + \lambda\dot{v} + \beta v + \kappa\ddot{x} = 0$.

Inverted beam harvester

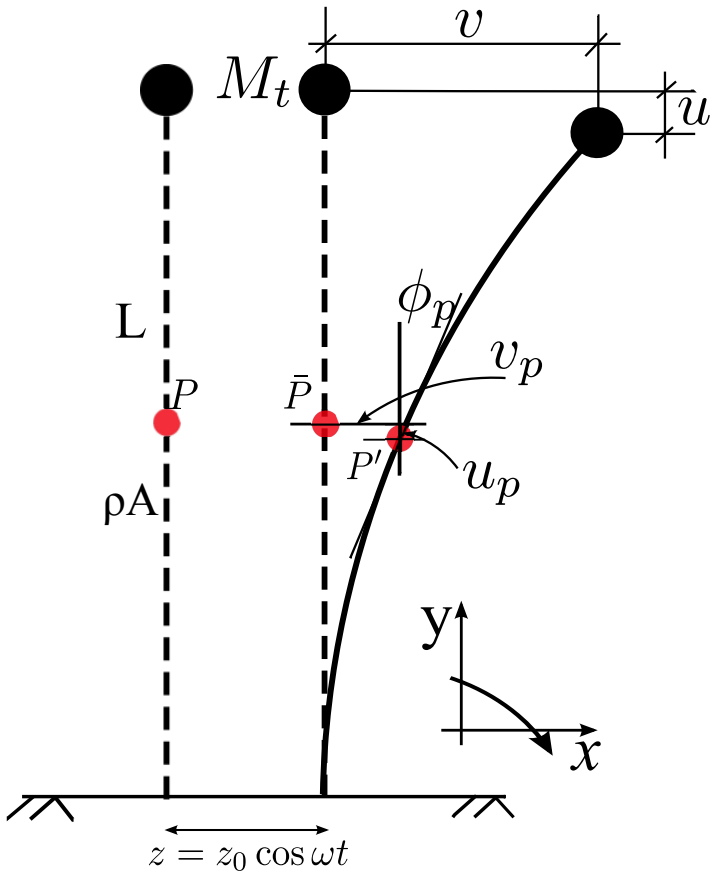

Schematic diagram of inverted beam harvester. Piezoelectric patches are placed along the beam but are not shown here.

The inverted beam-mass system

- For nonlinear energy harvesting, an inverted elastic beam is considered with a tip mass and the base is harmonically excited in the transverse direction.
- M_t denotes the tip mass attached to the elastic beam, while v and u denote the horizontal and vertical displacements of the mass. Point P denotes an arbitrary point on the beam whosse position is described by the coordinates s, v_p, and u_p.
- The displacement-curvature relation of the beam is nonlinear due to the large transverse displacement of the beam.
- We assume that the thickness of the beam is small compared with the length so that the effects of shear deformation and rotatory inertia of the beam can be neglected.
- The beam is such that the first torsional resonance frequency is much higher than the excitation frequency and the lumped mass is kept symmetric with respect to the centre line.

The inverted beam-mass system

- Hence the vibration is purely planar and we neglect the torsional modes of the beam in the analysis.
- These assumptions are consistent with observations in the laboratory.
- Consider an arbitrary point on the beam, P, at a distance s from the base. This point undergoes a rigid body translation due to the base excitation, and a further displacement due to the elastic beam deformation, given by $(v_p(s,t), -u_p(s,t))$.
- Hence the point P has undergone a total horizontal displacement of $z + v_p$, and a vertical displacement of $-u_p$.
- Let $\phi_p(s,t)$ denote the rotation of the beam at s, and hence the rotation at the tip mass is $\phi(t) = \phi_p(L_t, t)$, measured at the mass centre.
- The beam has a uniform cross sectional area A, mass density ρ, equivalent Young's modulus E, and second moment of area I.

Nonlinear equation of motion

- The kinetic energy of the beam-mass system is given by

$$T = \frac{1}{2}\rho A \int_0^L \left[(\dot{v}_p(s,t) + \dot{z})^2 + (\dot{u}_p(s,t))^2\right] \mathrm{d}s + \frac{1}{2}M_t\left[(\dot{v} + \dot{z})^2 + \dot{u}^2\right] + \frac{1}{2}I_t\dot{\phi}^2 \quad (3)$$

  where the translation of the tip mass is $v(t) = v_p(L_t, t)$ and $u(t) = u_p(L_t, t)$ and the dot denotes differentiation with respect to time. (3) is obtained by neglecting the effect of rotary inertia of the beam mass.

- The potential energy of the system is

$$\Pi = \frac{1}{2}EI \int_0^L (\kappa(s,t))^2 \mathrm{d}s - \rho A g \int_0^L u_p(s,t)\mathrm{d}s - M_t g u \quad (4)$$

Nonlinear equation of motion

- The curvature is given by

$$\kappa(s,t) = \frac{\partial \phi_p}{\partial s} = \phi_p' \tag{5}$$

the prime denotes differentiation with respect to s, and g is the gravitational constant.

- The slope of the beam, ϕ_p, may be written in terms of the beam elastic displacement as

$$\cos\phi_p = 1 - u_p' \quad \text{or} \quad \sin\phi_p = v_p' \tag{6}$$

- Hence

$$u_p' = 1 - \sqrt{1 - v_p'^2} \approx \frac{1}{2} v_p'^2 \quad \text{or} \quad u_p(s,t) = \frac{1}{2}\int_0^s (v_p'(\xi,t))^2 \mathrm{d}\xi \tag{7}$$

Nonlinear equation of motion

- The second of (6) gives

$$\phi_p(s,t) = \sin^{-1} v_p' \approx v_p' + \frac{1}{6} v_p'^3 \tag{8}$$

- Differentiating this equation gives

$$\kappa(s,t) = \phi_p' = \frac{v_p''}{\cos\phi_p} = \frac{v_p''}{\sqrt{1 - v_p'^2}} \approx v_p'' \left(1 + \frac{1}{2} v_p'^2\right) \tag{9}$$

Equations (7) - (9) have been expanded as Taylor series and the terms in $O(v_p^4)$ and higher orders neglected.

Nonlinear equation of motion

- To enforce nonlinearity, we assume that the tip mass is significantly larger than the beam mass and hence a single mode approximation of the beam deformation is sufficient.
- The displacement at any point in the beam is represented as a function of the tip mass displacement through a function for the beam deformation, $\psi(s)$, as

$$v_p(s,t) = v_p(L,t)\psi(s) = v(t)\psi(s) \tag{10}$$

- The displacement may be approximated by any function satisfying the boundary conditions at $s = 0$

$$\psi(s) = \lambda_t \left(1 - \cos\left(\frac{\pi s}{2L}\right)\right) \tag{11}$$

where λ_t is a constant such that $\psi(L_t) = 1$, i.e.

$$\lambda_t = 1/\left(1 - \cos\left(\frac{\pi L_t}{2L}\right)\right) \tag{12}$$

Nonlinear equation of motion

- Using this single mode approximation, the kinetic energy of the system in terms of the transverse displacement of the tip mass, v is

$$
\begin{aligned}
T =& \frac{1}{2}\rho A \int_0^L \left[(\dot{v}\psi(s) + \dot{z})^2 + \left(v\dot{v} \int_0^s (\psi'(\xi))^2 \mathrm{d}\xi \right)^2 \right] \mathrm{d}s \\
&+ \frac{1}{2} M_t \left[(\dot{v} + \dot{z})^2 + \left(v\dot{v} \int_0^{L_t} (\psi'(s))^2 \mathrm{d}s \right)^2 \right] \\
&+ \frac{1}{2} I_t \left[\dot{v}\psi'(L_t) + \frac{1}{2} v^2 \dot{v} (\psi'(L_t))^3 \right]^2 \qquad (13) \\
=& \frac{1}{2}\rho A \left[N_1 \dot{v}^2 + 2N_2 \dot{v}\dot{z} + \dot{z}^2 L + N_3 \left(v\dot{v} \right)^2 \right] \\
&+ \frac{1}{2} M_t \left[(\dot{v} + \dot{z})^2 + N_4^2 \left(v\dot{v} \right)^2 \right] + \frac{1}{2} I_t \left[N_5 \dot{v} + \frac{1}{2} N_5^3 v^2 \dot{v} \right]^2 \qquad (14)
\end{aligned}
$$

Nonlinear equation of motion

- Using this single mode approximation, the potential energy of the system in terms of the transverse displacement of the tip mass, v is

$$\Pi = \frac{1}{2}EI\int_0^L \left[v\psi(s)'' + \frac{1}{2}v^3(\psi'(s))^2\psi''(s)\right]^2 \mathrm{d}s - \frac{1}{2}\rho A g v^2 \int_0^L \left[\int_0^s (\psi'(\xi))^2 \mathrm{d}\xi\right] \mathrm{d}s - \frac{1}{2}M_t g v^2 \int_0^{L_t} (\psi'(s))^2 \mathrm{d}s \tag{15}$$

$$= \frac{1}{2}EI\left[N_6 v^2 + N_7 v^4 + \frac{1}{4}N_8 v^6\right] - \frac{1}{2}N_9 \rho A g v^2 - \frac{1}{2}N_4 M_t g v^2 \tag{16}$$

Nonlinear equation of motion

- Using the displacement model in (11), the constants N_1 to N_9 are:

$$
\begin{aligned}
N_1 &= \int_0^L (\psi(s))^2 \mathrm{d}s = \lambda_t^2 \left(\frac{3\pi - 8}{2\pi}\right) L, \\
N_2 &= \int_0^L \psi(s) \mathrm{d}s = \lambda_t \left(\frac{\pi - 2}{\pi}\right) L, \\
N_3 &= \int_0^L \left(\int_0^s (\psi'(\xi))^2 \mathrm{d}\xi\right)^2 \mathrm{d}s = \lambda_t^2 \left(\frac{\pi^2(2\pi^2 - 9)}{384}\right) \frac{1}{L}, \\
N_4 &= \int_0^{L_t} (\psi'(s))^2 \mathrm{d}s = \lambda_t^2 \left(\frac{\pi^2}{8}\right) \frac{1}{L_t}, \\
N_5 &= \psi'(L_t) = \lambda_t \left(\frac{\pi}{2}\right) \frac{1}{L_t}, \\
N_6 &= \int_0^L (\psi''(s))^2 \mathrm{d}s = \lambda_t^2 \left(\frac{\pi^4}{32}\right) \frac{1}{L^3} \\
N_7 &= \int_0^L (\psi'(s)\psi''(s))^2 \mathrm{d}s = \lambda_t^4 \left(\frac{\pi^6}{2^9}\right) \frac{1}{L^5} \\
N_8 &= \int_0^L (\psi'(s))^4 (\psi''(s))^2 \mathrm{d}s = \lambda_t^6 \left(\frac{\pi^8}{4096}\right) \frac{1}{L^7} \\
N_9 &= \int_0^L \left[\int_0^s (\psi'(\xi))^2 \mathrm{d}\xi\right] \mathrm{d}s = \lambda_t^2 \left(-\frac{1}{4} + \frac{1}{16}\pi^2\right)
\end{aligned}
\tag{17}
$$

Nonlinear equation of motion

- The equation of motion of the beam-mass system is derived in terms of the displacement of the tip mass using Lagrange's equations as

The equation of motion:

$$\begin{aligned}\left[N_5^2 I_t + M_t + \rho A N_1 + \left(\rho A N_3 + M_t N_4^2 + N_5^4 I_t\right) v^2\right] \ddot{v} \\ + \left[\rho A N_3 + M_t N_4^2 + N_5^4 I_t\right] v \dot{v}^2 \\ + \left[EIN_6 - N_9 \rho A g - N_4 M_t g + 2EIN_7 v^2\right] v = \\ - \left[\rho A N_2 + M_t\right] \ddot{z} \quad (18)\end{aligned}$$

- Damping may also be added to these equations of motion, for example viscous, material or aerodynamic damping. This will introduce additional terms involving $\dot{v}$.

Equilibrium points

- The equilibrium positions with no forcing are obtained by setting the velocity and acceleration terms to zero in (18) to give,

$$\left[EIN_6 - N_9\rho Ag - N_4M_tg + 2EIN_7v^2\right]v = 0 \tag{19}$$

- This equation has either one or three solutions, and $v = 0$ is always a solution. Since $N_4 > 0$, there are three solutions if

$$M_t > \frac{EIN_6 - N_9\rho Ag}{N_4g} = M_{tb} \tag{20}$$

  where M_{tb} is the tip mass so that the beam is about to buckle.
- If the beam mass is neglected this gives the Euler buckling load as

$$M_{tb}g = \frac{EIN_6}{N_4} = \frac{EI\pi^2}{4L^2} \tag{21}$$

Equilibrium points

- If (20) is satisfied then the non-zero equilibrium positions are given by

$$v_{0b} = \pm\sqrt{\frac{N_9\rho Ag + N_4 M_t g - EIN_6}{2EIN_7}} \tag{22}$$

- For perturbations about the equilibrium solution at $v = 0$ the linearized equation of motion for the free response is

$$\left[N_5^2 I_t + M_t + \rho A N_1\right]\ddot{v} + \left[EIN_6 - N_9\rho Ag - N_4 M_t g\right]v = 0 \tag{23}$$

  showing that the $v = 0$ equilibrium position is unstable after buckling $(M_t > M_{tb})$.
- Before buckling $(M_t < M_{tb})$ the natural frequency for small vibrations is given by

ω_n

$$\omega_n^2 = \frac{EIN_6 - N_9\rho Ag - N_4 M_t g}{N_5^2 I_t + M_t + \rho A N_1} \tag{24}$$

Equilibrium points

- After bucking the linearized equation of motion about the equilibrium position v_{0b} becomes, using (22),

$$\left[N_5^2 I_t + M_t + \rho A N_1 + \left(\rho A N_3 + M_t N_4^2 + N_5^4 I_t\right) v_{0b}^2\right] \ddot{\eta} + 4EIN_7 v_{0b}^2 \eta = 0 \quad (25)$$

  where $v = v_{0b} + \eta$.
- Hence the natural frequencies about both buckled equilibrium position are

ω_{nb}

$$\omega_{nb}^2 = \frac{4EIN_7 v_0^2}{N_5^2 I_t + M_t + \rho A N_1 + \left(\rho A N_3 + M_t N_4^2 + N_5^4 I_t\right) v_{0b}^2} \quad (26)$$

Coupled electromechanical model

- There has been a significant modeling effort of piezoelectric materials as distributed transducers and many review papers have been published.
- Suppose that piezoelectric layers added to a beam in either a unimorph or a bimorph configuration. Then the moment about the beam neutral axis produced by a voltage V across the piezoelectric layers may be written as

$$M(x,t) = \gamma_c V(t) \tag{27}$$

- The constant γ_c depends on the geometry, configuration and piezoelectric device and $V(t)$ is the time-dependent voltage.
- For a bimorph with piezoelectric layers in the 31 configuration, with thickness h_c, width b_c and connected in parallel

$$\gamma_c = E d_{31} b_c \left(h + h_c\right) \tag{28}$$

where h is the thickness of the beam and d_{31} is the piezoelectric constant.

Coupled electromechanical model

- For a unimorph, the constant is

$$\gamma_c = E d_{31} b_c \left(h + \frac{h_c}{2} - \bar{z} \right) \tag{29}$$

  where $\bar{z}$ is the effective neutral axis
- These expressions assume a monolithic piezoceramic actuator perfectly bonded to the beam.
- The work done by the piezoelectric patches in mov- ing or extracting the electrical charge is

$$W = \int_0^{L_c} M(x,t)\kappa(x)\mathrm{d}x \tag{30}$$

  where L_c is the active length of the piezoelectric material, which is assumed to be attached at the clamped end of the beam.

Coupled electromechanical model

- The quantity $\kappa(x)$ is the curvature of the beam and this is approximately expressed in
- Using the approximation for κ in (8), and the displacement model in (10), we have

$$W \approx \left(\Theta_1 v + \frac{1}{3}\Theta_2 v^3\right) V \tag{31}$$

where

$$\Theta_1 = \gamma_c \int_0^{L_c} \psi''(s)\mathrm{d}s = \gamma_c \psi'(L_c) \tag{32}$$

and

$$\Theta_2 = 3\gamma_c \int_0^{L_c} \frac{1}{2}\psi''(s)(\psi'(s))^2\mathrm{d}s = \frac{1}{2}\gamma_c(\psi'(L_c))^3. \tag{33}$$

Coupled electromechanical model

- Equation (31) results in additional terms in the mechanical equations of motion, which becomes

$$\begin{aligned}\left[N_5^2 I_t + M_t + \rho A N_1 + \left(\rho A N_3 + M_t N_4^2 + N_5^4 I_t\right) v^2\right] \ddot{v} \\ + \left[\rho A N_3 + M_t N_4^2 + N_5^4 I_t\right] v \dot{v}^2 \\ + \left[EI N_6 - N_9 \rho A g - N_4 M_t g + 2EI N_7 v^2\right] v \\ - \Theta_1 V - \Theta_2 v^2 V = -\left[\rho A N_2 + M_t\right] \ddot{z}. \quad (34)\end{aligned}$$

- On the electrical side the piezoelectric patches may be considered as a capacitor, and the charge they produce is given by $\Theta_1 v + \Theta_2 v^3$ where Θ_1 and Θ_2 are given by (32) and (33), respectively.

Coupled electromechanical model

- The electrical circuit considered is represented by a resistive shunt connected across the piezoelectric patch. The electrical equation then becomes

$$C_p\dot{V} + \frac{V}{R_l} + \Theta_1\dot{v} + \Theta_2 v^2\dot{v} = 0 \tag{35}$$

where R_l is the load resistor and C_p is the capacitance of the piezoelectric patch.
The average power scavenged between times T_1 and T_2 is calculated as

$$P_{ave} = \frac{1}{T_2 - T_1}\int_{T_1}^{T_2} \frac{V(t)^2}{R_l}\mathrm{d}t. \tag{36}$$

Parameter values

Table: Parameter values used in the simulation

Beam and Tip Mass			Energy Harvester		
ρ	7850	kg/m^3	L_c	28	mm
E	210	GN/m^2	b_c	14	mm
b	16	mm	h_c	300	μm
h	0.254	mm	γ_c	-4.00×10^{-5}	Nm/V
$L = L_t$	300	mm	C_p	51.4	nF
I_t/M_t	40.87	mm^2	R_l	$10^5 - 10^8$	Ω

- The beam-mass system is excited at the base with harmonic excitation.
- When the tip mass is changed the ratio of M_t/I_t is maintained; this is equivalent to increasing the tip mass width to increase the tip mass.

Numerical simulation results

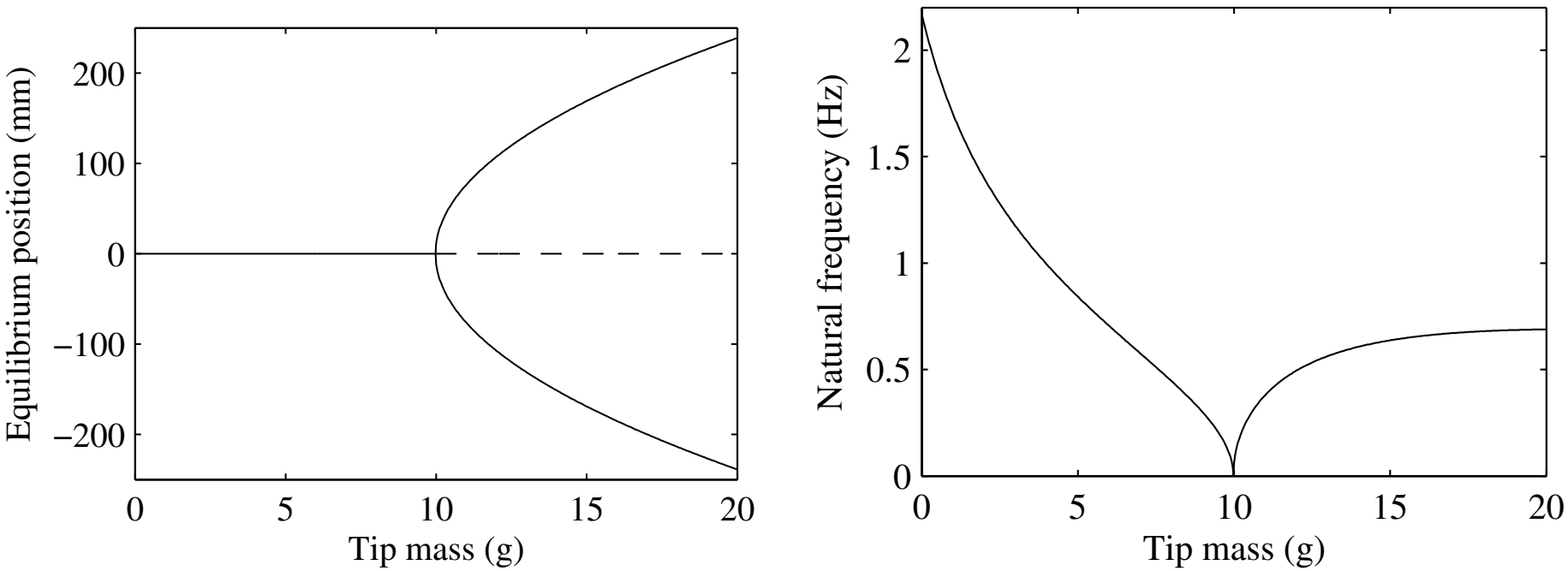

(a) Equilibrium position

(b) Natural frequency

Figure: The effect of the tip mass on the equilibrium position and the corresponding natural frequencies for the stable equilibrium positions. The dashed line denotes unstable equilibrium positions.

Numerical simulation results

- Figure 1(a) shows the equilibrium position of the tip mass, using the analysis described in Section 2, and shows that the post buckled response has two equilibrium positions.
- Figure 1(b) shows the corresponding natural frequency of the linearized system with the change in the tip mass; both the pre-buckled and post-buckled natural frequencies are given.
- Linearization about both equilibrium positions provides the same natural frequencies as the system is assumed to be symmetric.
- Figure 1(b) shows that the natural frequency of the inverted elastic pendulum decreases with increasing tip mass and is zero at the Euler buckling load corresponding to an estimated tip mass of 10.0g.

Numerical simulation results

- Further increases in tip mass cause the beam to buckle and the natural frequencies about the stable equilibrium positions increase with the tip mass. Thus the inverted elastic beam-mass system is able to resonate at a low frequencies close to the buckling condition.
- The post-buckled equilibrium positions are quite sensitive to the tip mass and in the simulation study a tip mass of 10.5g was used, unless stated otherwise.

Numerical simulation results

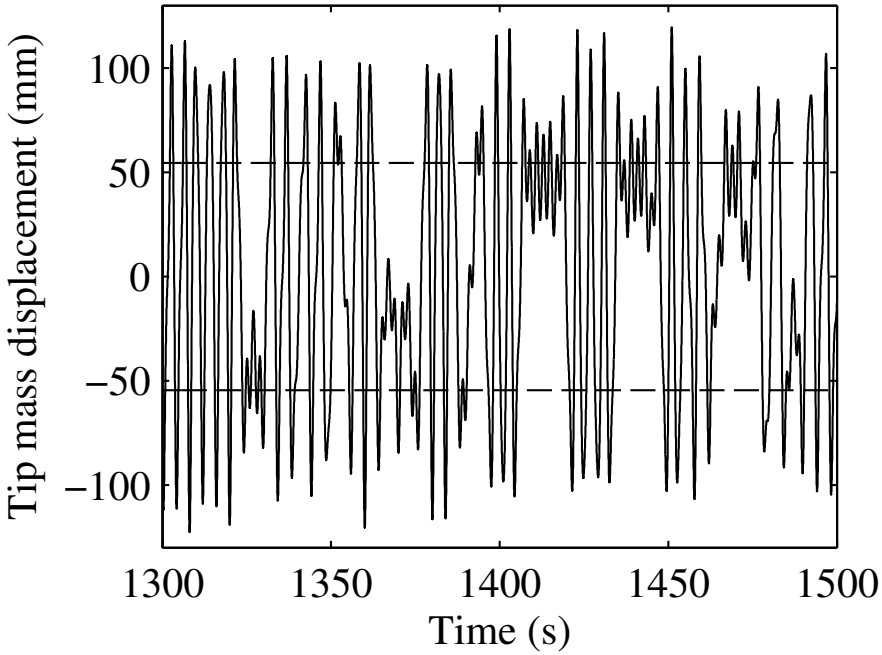

(a) Displacement time history

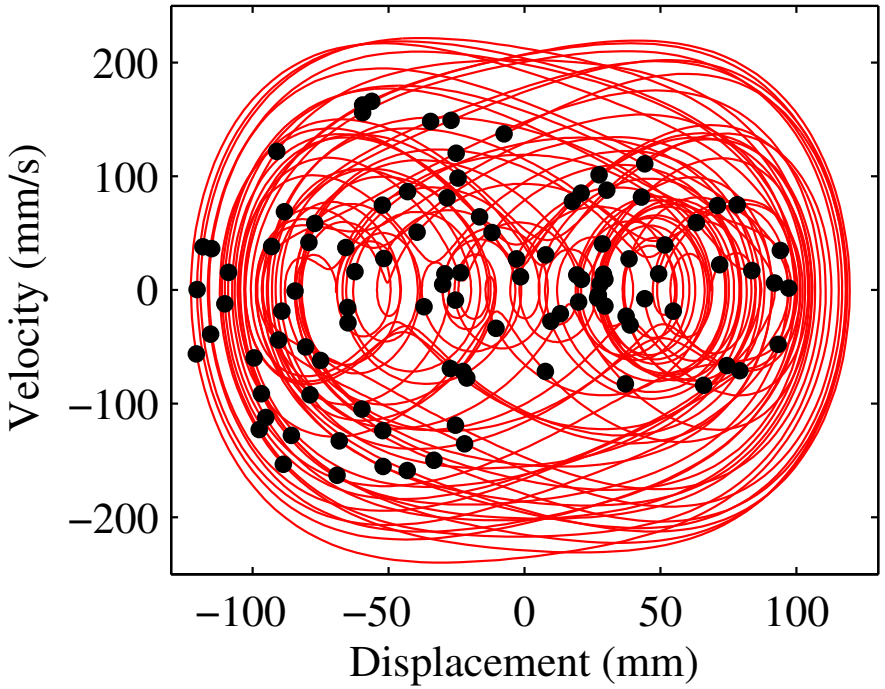

(b) Phase portrait for the tip mass

Figure: Harvester nonperiodic response for the parameters given in Table 1 and an harmonic excitation with $z_0 = 16$mm at frequency 0.5Hz. The dashed horizontal lines in (a) show the equilibrium positions of the tip mass. The dots in (b) represent the Poincaré points. The response was obtained using zero initial conditions for the tip mass displacement and velocity.

Numerical simulation results

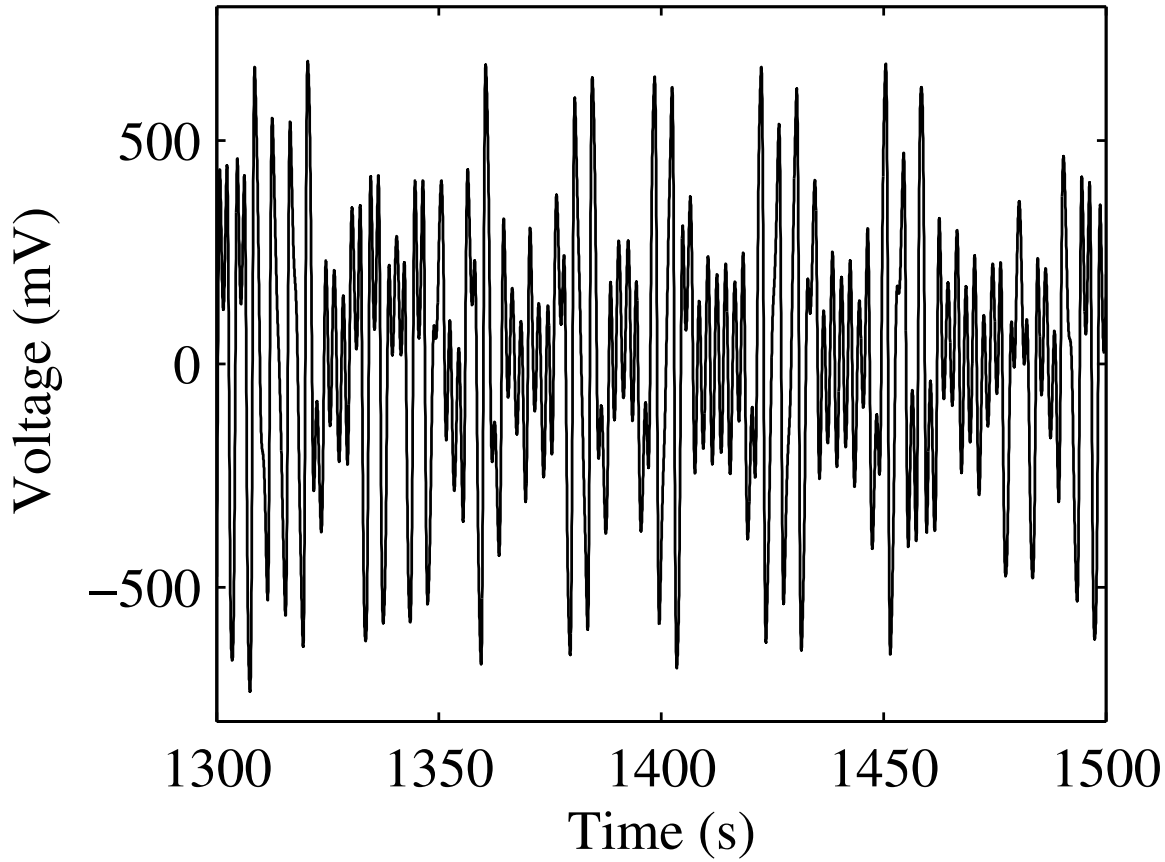

Figure: Time history of the voltage across the piezoelectric layers with the parameters given in Table 1 and corresponding to the response given in Figure 2.

Numerical simulation results

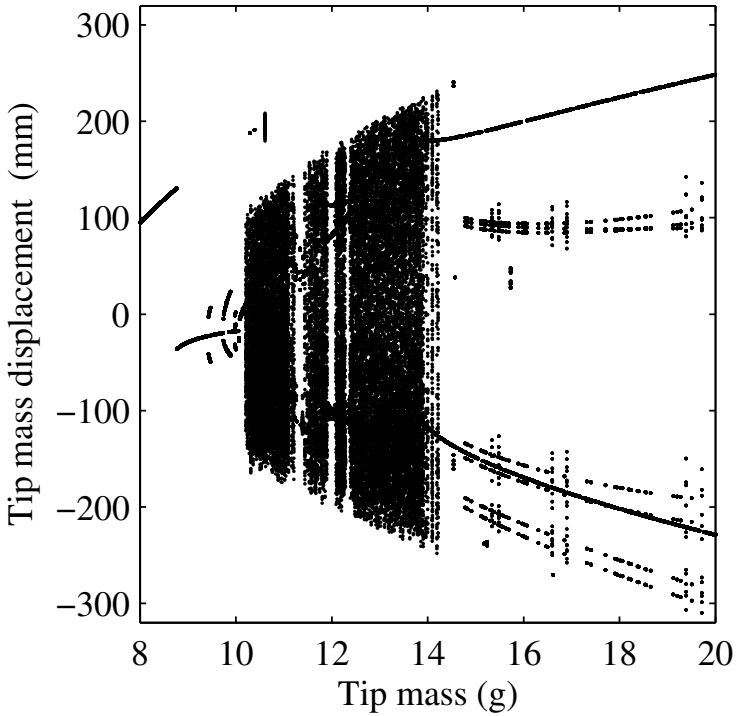

(a) Bifurcation diagram

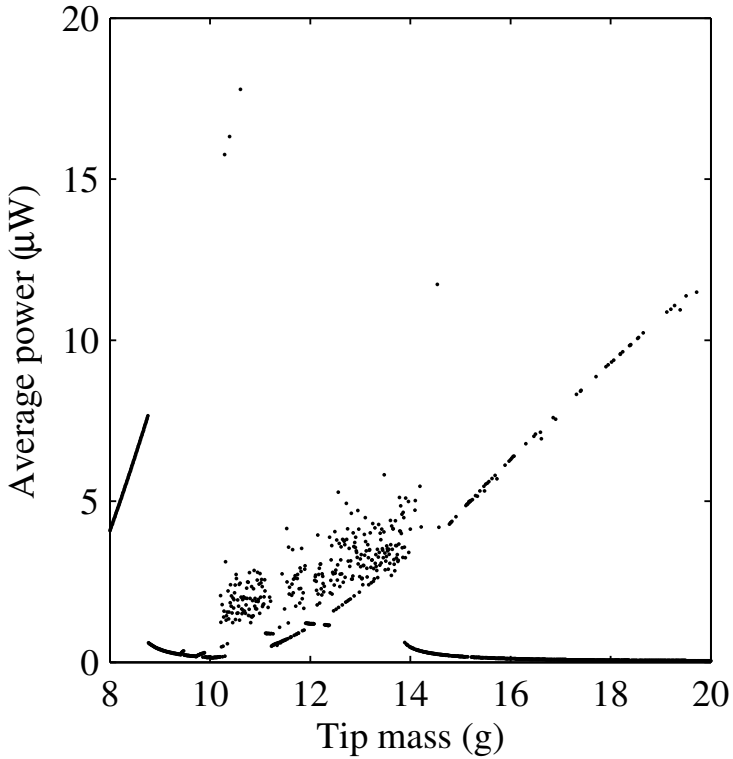

(b) Average harvested power

Figure: The effect of the variation of the tip mass for a base excitation of $z_0 = 16$mm at frequency 0.5Hz, and for a load resistance $R_l = 100\text{k}\Omega$. The results were obtained using zero initial conditions for the tip mass displacement and velocity.

Numerical simulation results

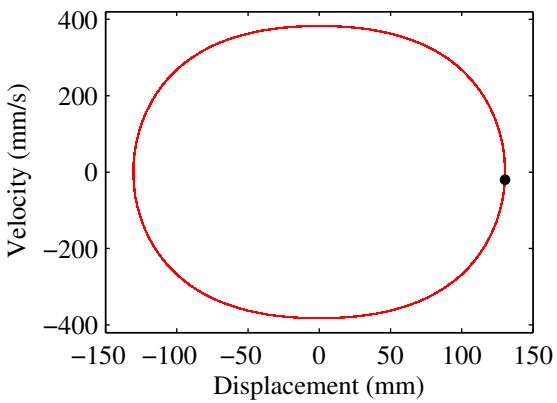

(a) $M_t = 8.76\text{g}$, $P_{ave} = 7.65\mu\text{W}$

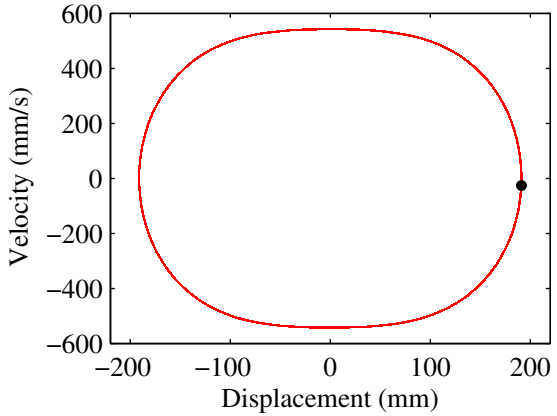

(b) $M_t = 10.39\text{g}$, $P_{ave} = 16.3\mu\text{W}$

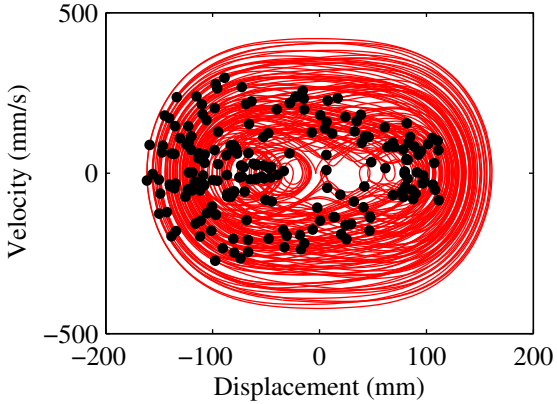

(c) $M_t = 10.5\text{g}$, $P_{ave} = 2.40\mu\text{W}$

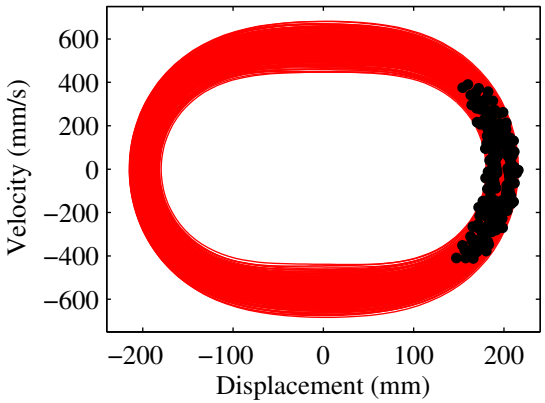

(d) $M_t = 10.61\text{g}$, $P_{ave} = 17.8\mu\text{W}$

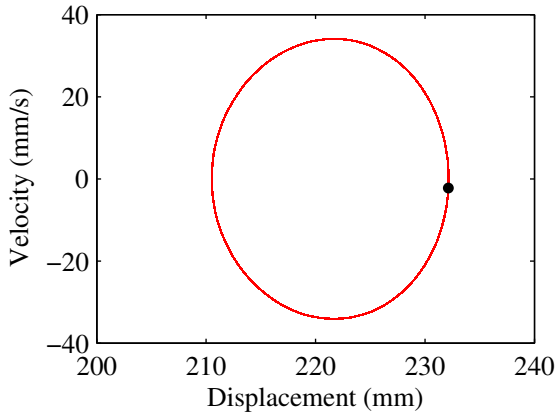

(e) $M_t = 18.6\text{g}$, $P_{ave} = 0.056\mu\text{W}$

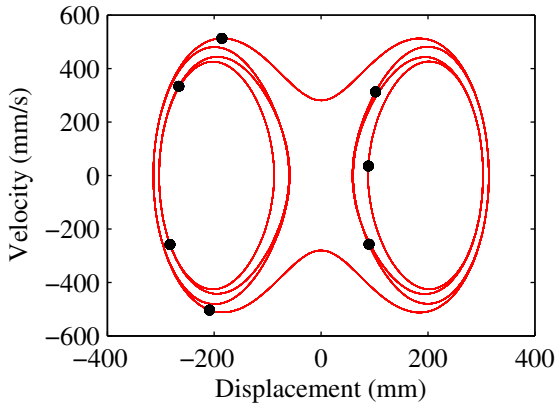

(f) $M_t = 18.65\text{g}$, $P_{ave} = 10.2\mu\text{W}$

Figure: Phase portraits of the tip mass response for a base excitation of $z_0 = 16\text{mm}$ at frequency 0.5Hz, and for a load resistance $R_l = 100\text{k}\Omega$.

Numerical simulation results

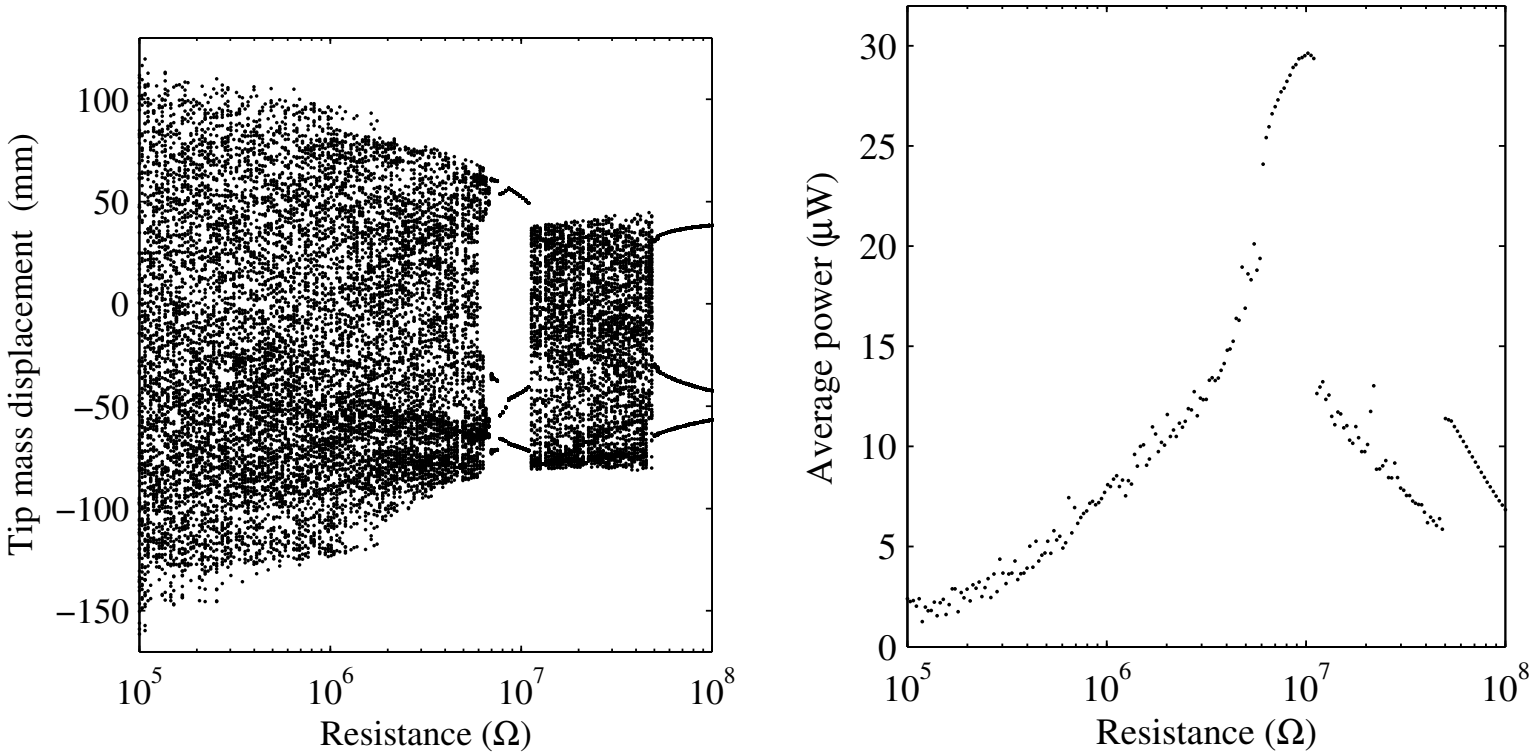

(a) Bifurcation diagram

(b) Average harvested power

Figure: The effect of the resistance across the piezoelectric layer, for a tip mass of $M_t = 10.5$g, and a base excitation of amplitude $z_0 = 16$mm at frequency $\omega = 0.5$Hz. The results were obtained using zero initial conditions for the tip mass displacement and velocity.

Numerical simulation results

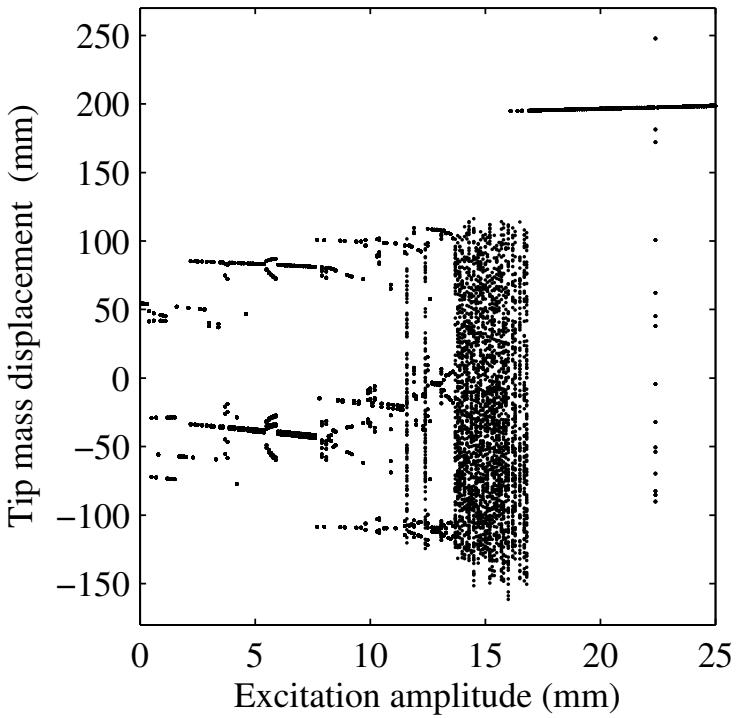

(a) Bifurcation diagram

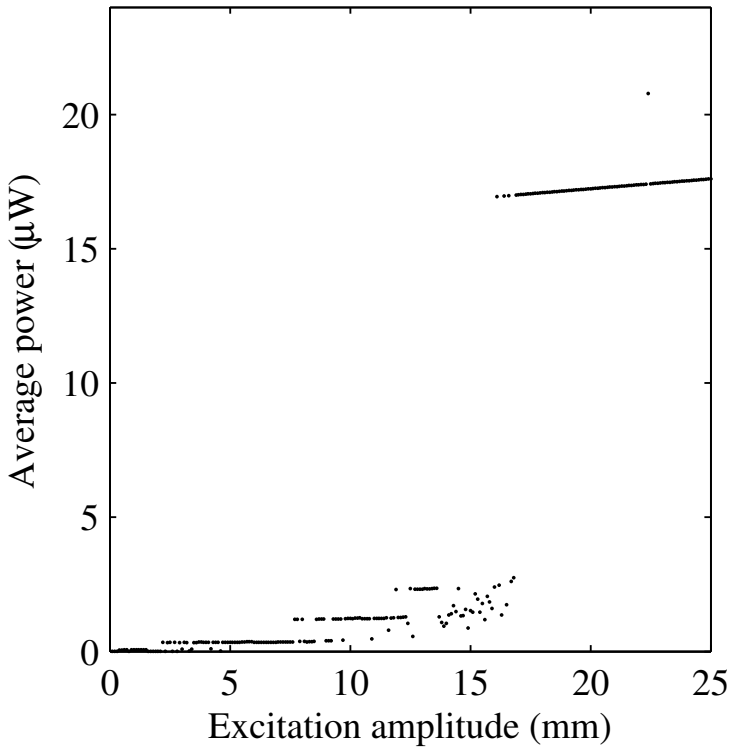

(b) Average harvested power

Figure: The effect of the amplitude of the base excitation at an excitation frequency of 0.5Hz, a tip mass of $M_t = 10.5$g and a load resistance $R_l = 100$kΩ. The results were obtained using zero initial conditions for the tip mass displacement and velocity.

Numerical simulation results

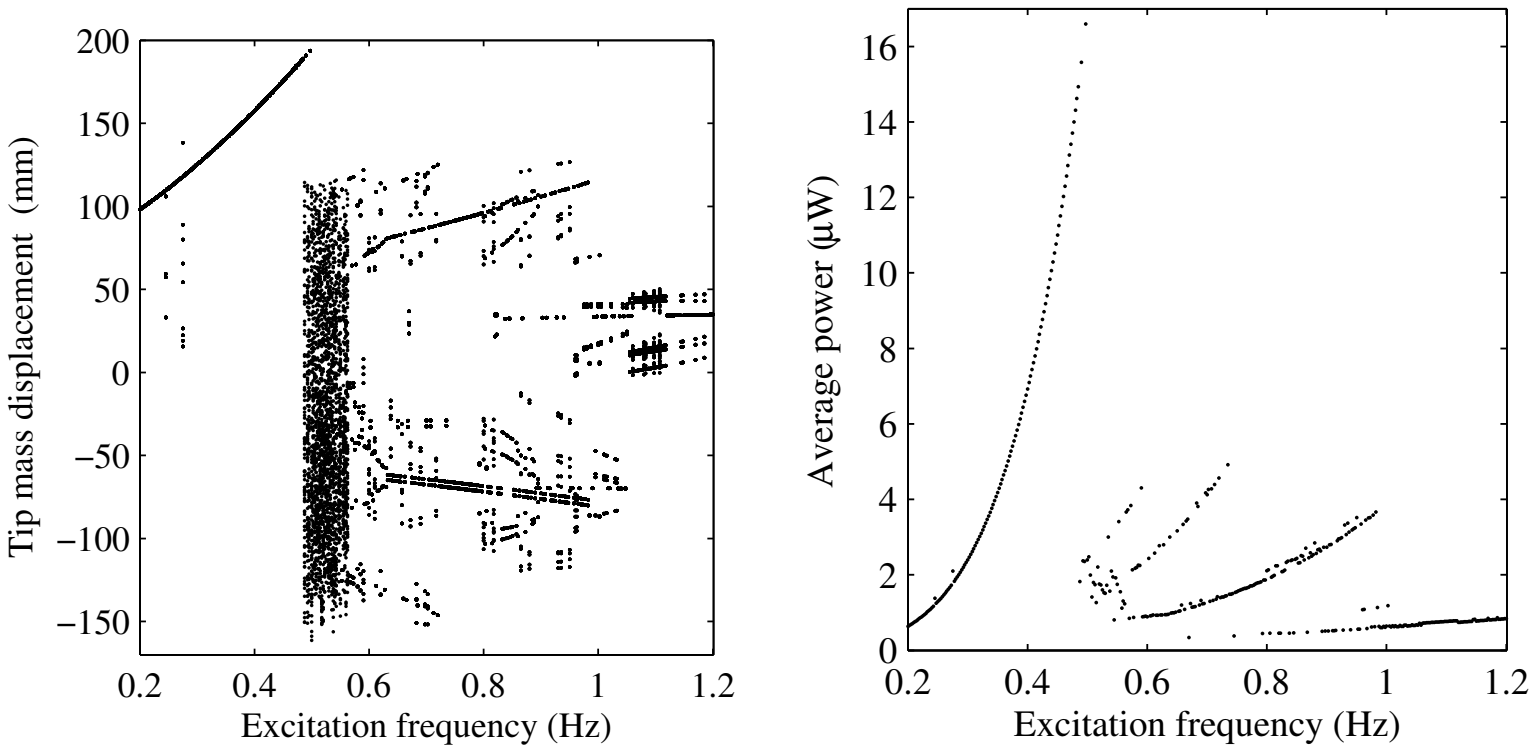

(a) Bifurcation diagram

(b) Average harvested power

Figure: The effect of the frequency of the base excitation for an excitation amplitude of $z_0 = 16$mm, a tip mass of $M_t = 10.5$g and a load resistance $R_l = 100\text{k}\Omega$. The results were obtained using zero initial conditions for the tip mass displacement and velocity.

Experimental set up

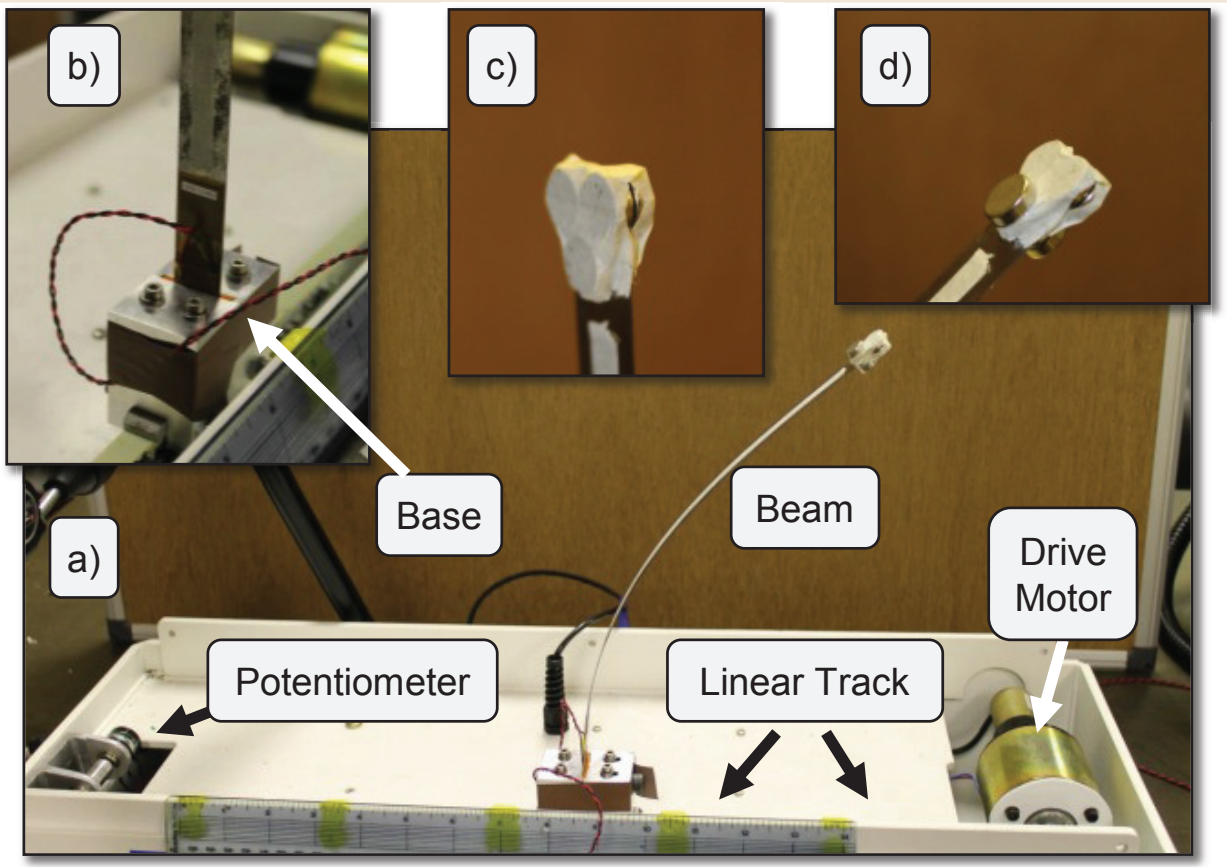

Figure: Picture of the experimental setup. a) Linear slider and the inverted cantilever beam with 14.0 g tip mass. b) Base of the beam showing the MFC device. c) Tip mass of 10.5 g shown nearly vertical at the stable equilibrium. d) Tip mass of 14.0 g showing approximately 45° end slope in a stable equilibrium.

Experimental set up

Table: Resistor values used in the experiment.

Nominal resistance	Measured resistance at piezo output
10kΩ	9.91kΩ
100kΩ	99.3kΩ
150kΩ	146.9kΩ
330kΩ	318.3kΩ
450kΩ	450.6kΩ
1MΩ	910kΩ
1.5MΩ	1.658MΩ
2.2MΩ	2.272MΩ
3.3MΩ	3.344MΩ
Open	9.944MΩ

Experimental results

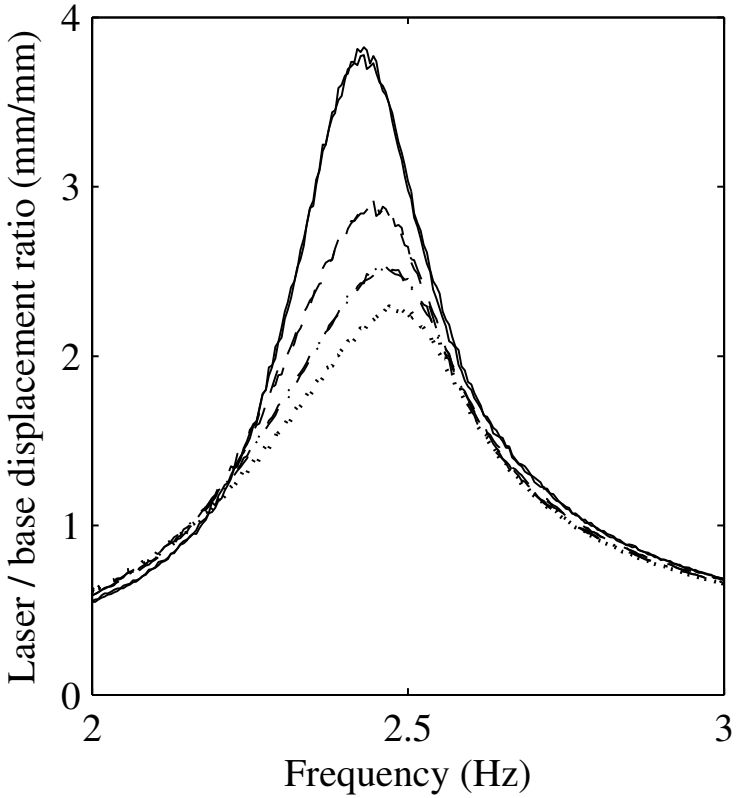

(a) Response measured by laser

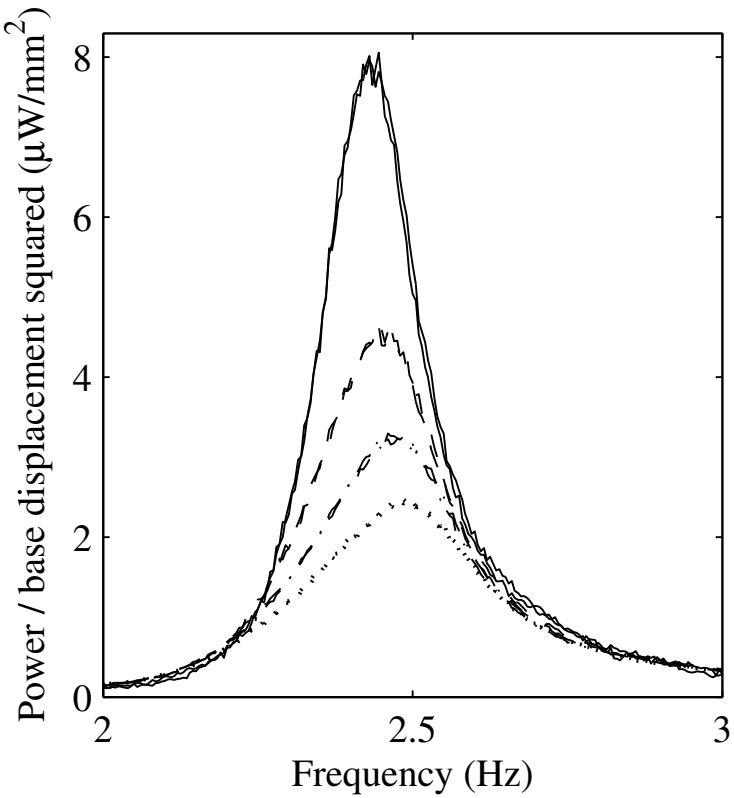

(b) Average harvested power

Figure: The experimental results for a tip mass of $M_t = 0$, and a base excitation with amplitudes of $z_0 = 5$ (solid), 10 (dashed), 15 (dash-dot) and 20 mm (dotted) at a range of frequencies. $R_l = 1.658\,\mathrm{M}\Omega$ for all measurements.

Experimental results

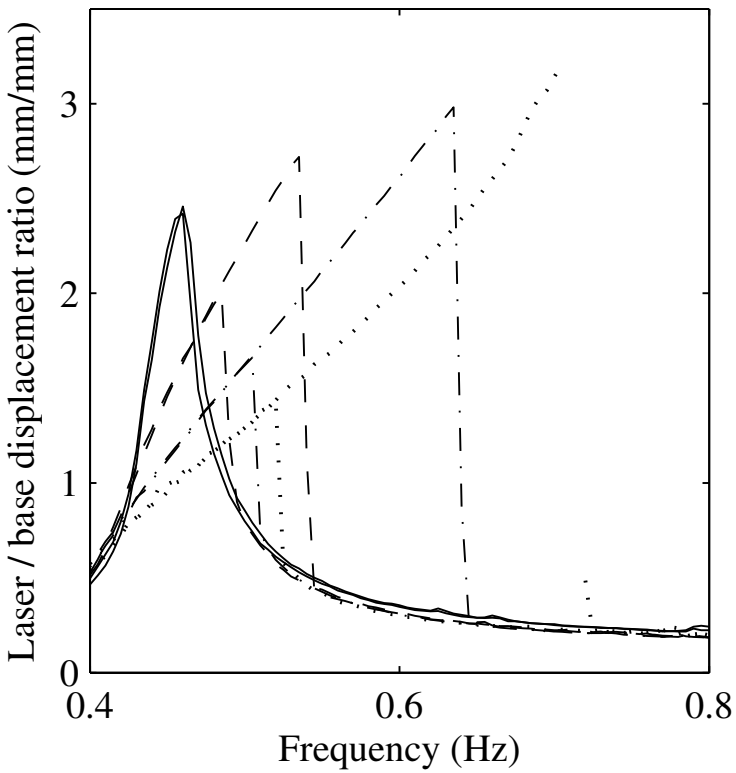

(a) Response measured by laser

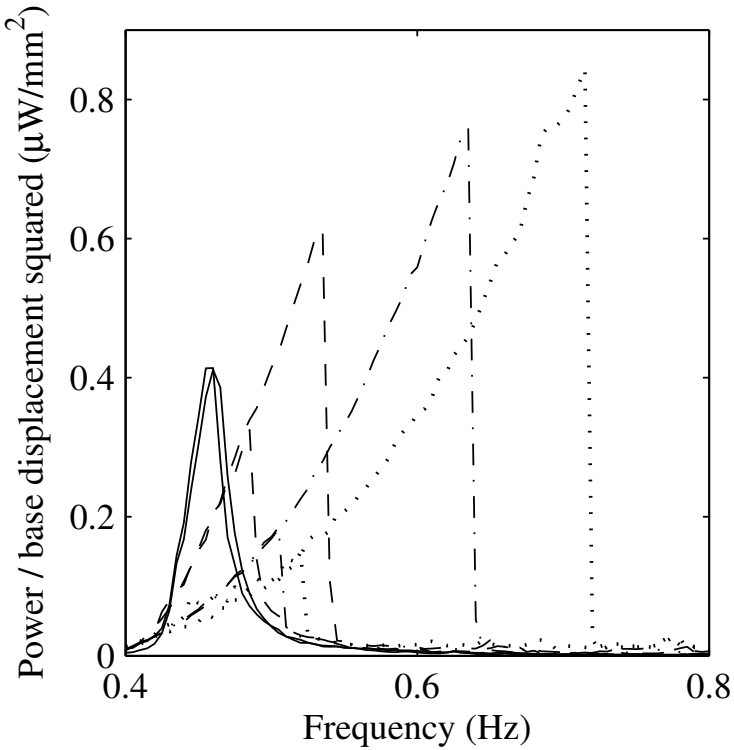

(b) Average harvested power

Figure: The experimental results for a tip mass of $M_t = 10.5$g, and a base excitation with amplitudes of $z_0 = 5$ (solid), 10 (dashed), 15 (dash-dot) and 20 mm (dotted) at a range of frequencies. $R_l = 9.944\,\mathrm{M}\Omega$ for $z_0 = 5$ and 10 mm, and $R_l = 3.344\,\mathrm{M}\Omega$ for $z_0 = 15$ and 20 mm.

Experimental results

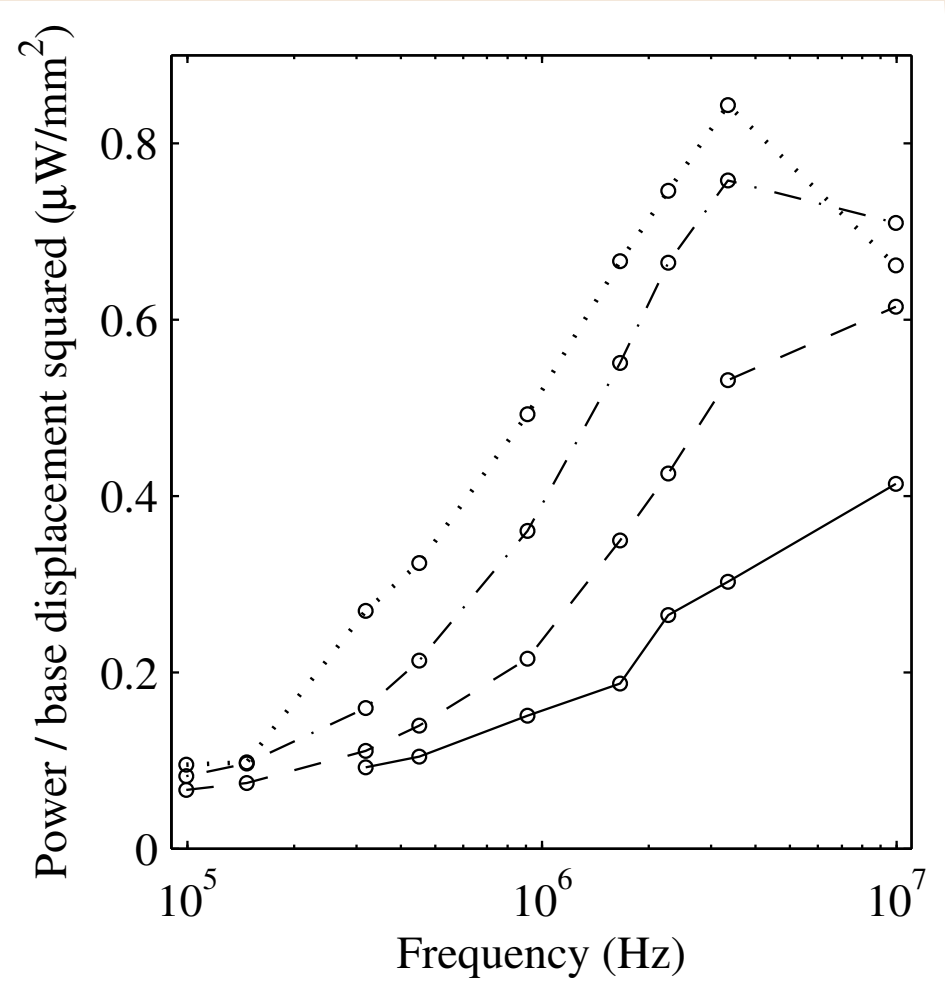

Figure: The experimental maximum power for a tip mass of $M_t = 10.5$g, and a base excitation with amplitudes of $z_0 = 5$ (solid), 10 (dashed), 15 (dash-dot) and 20 mm (dotted), for a range of load resistance.

Experimental results

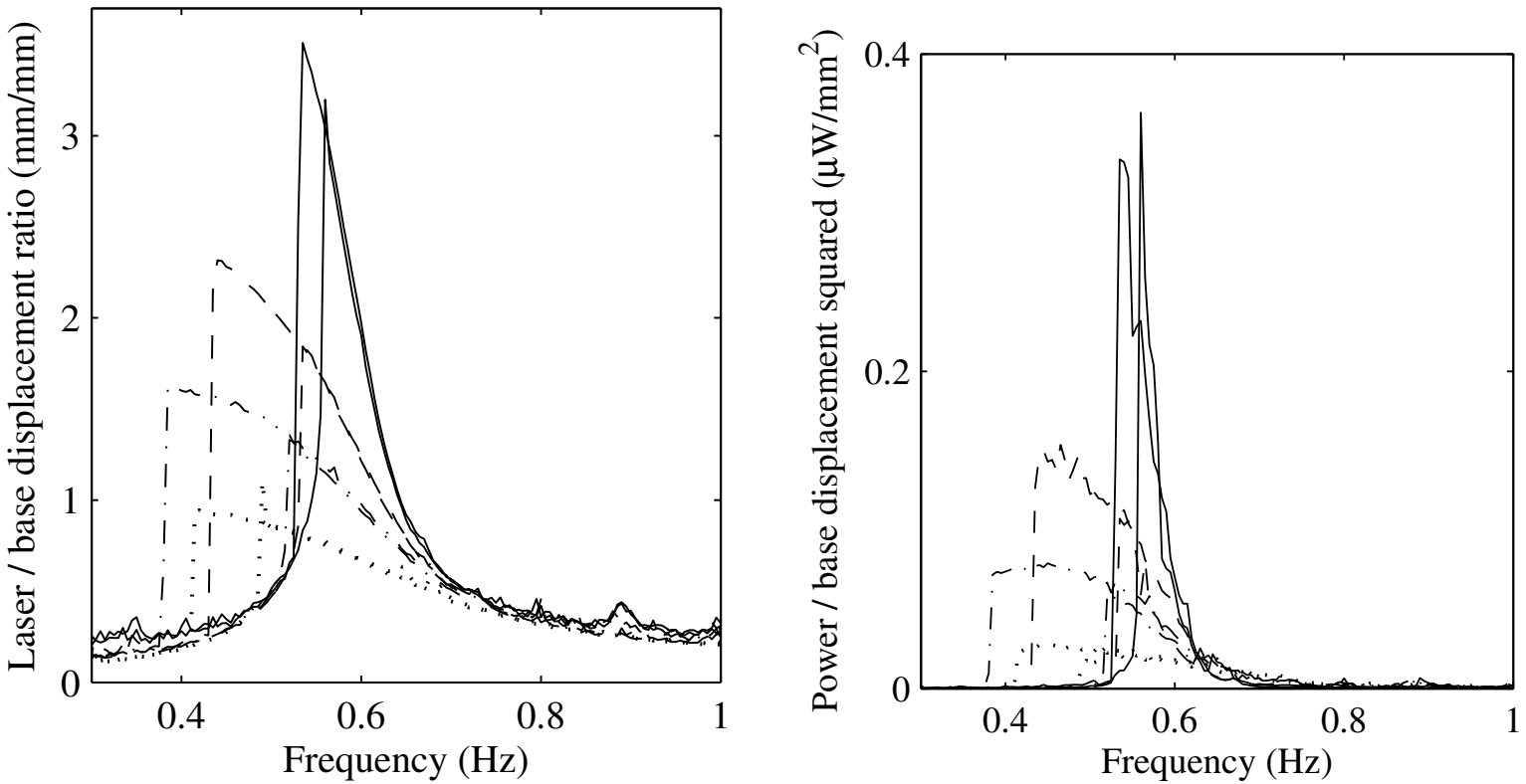

(a) Response measured by laser (b) Average harvested power

Figure: The experimental results for a tip mass of $M_t = 14$g, and a base excitation with amplitudes of $z_0 = 5$ (solid), 10 (dashed), 15 (dash-dot) and 25 mm (dotted) at a range of frequencies. $R_l = 9.944\,\mathrm{M}\Omega$.

Experimental system simulation

- The experimental system was modeled using the equations of motion of the inverted cantilever beam developed earlier in order to validate the model.
- There are two linked issues with simulating the tested system: the parameters of the model may only be obtained approximately from the geometry of the structure and the material properties; and the response is highly sensitive to the some parameters in the model.
- In addition, damping is very difficult to model and in reality will mainly consist of viscoelastic material damping and air damping. In the model a linear viscous damper has been included, where the coefficient varies with the response amplitude.
- The single piezoelectric patch adds significant stiffness to the beam and will also cause a shift in the neutral axis of the beam. This will also change the mode shapes of the beam and therefore the displacement function if taken as the first mode.

Simulated results

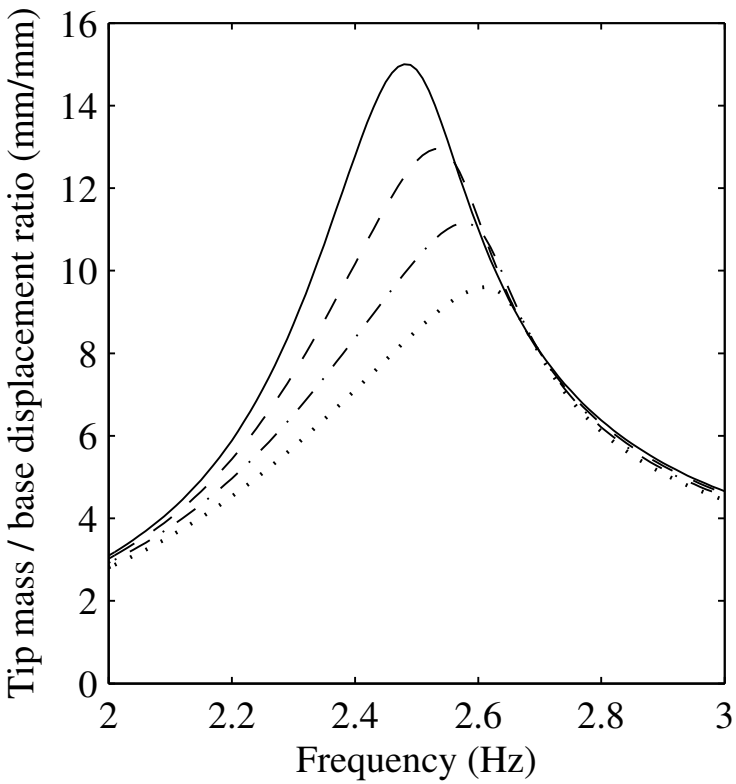

(a) Tip mass response

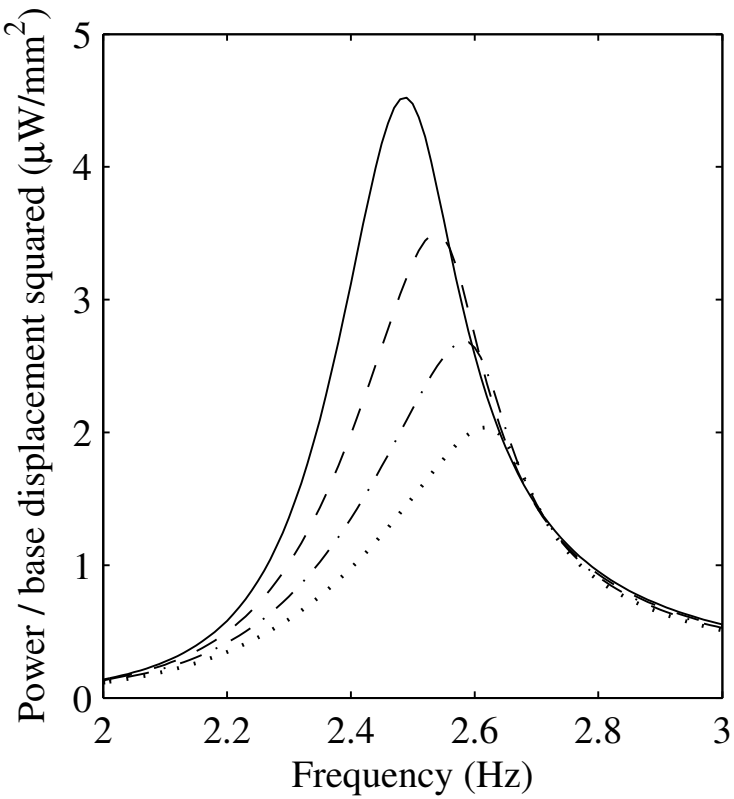

(b) Average harvested power

Figure: The simulated results for a tip mass of $M_t = 0$, and a base excitation with amplitudes of $z_0 = 5$ (solid), 10 (dashed), 15 (dash-dot) and 20 mm (dotted) at a range of frequencies. $R_l = 1.658\,\mathrm{M}\Omega$ for all cases.

Simulated results

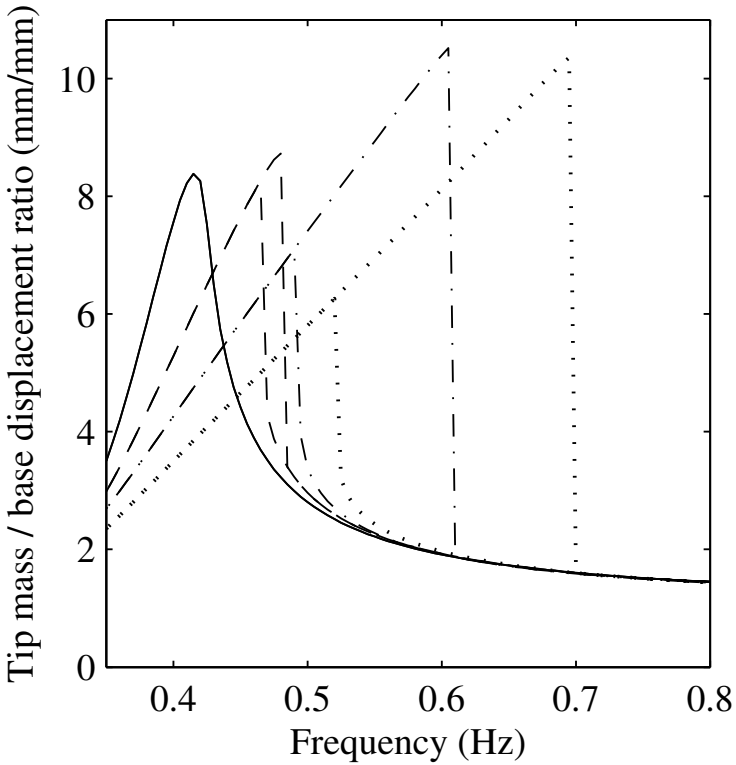

(a) Tip mass response

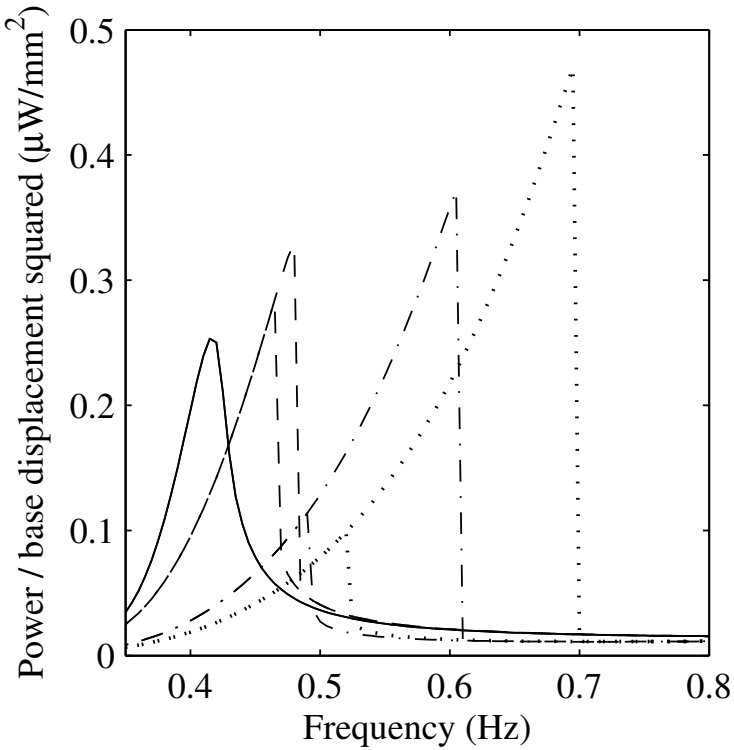

(b) Average harvested power

Figure: The simulated results for a tip mass of $M_t = 10.5$g, and a base excitation with amplitudes of $z_0 = 5$ (solid), 10 (dashed), 15 (dash-dot) and 20 mm (dotted) at a range of frequencies. $R_l = 9.944\,\mathrm{M}\Omega$ for $z_0 = 5$ and 10 mm, and $R_l = 3.344\,\mathrm{M}\Omega$ for $z_0 = 15$ and 20 mm.

Simulated results

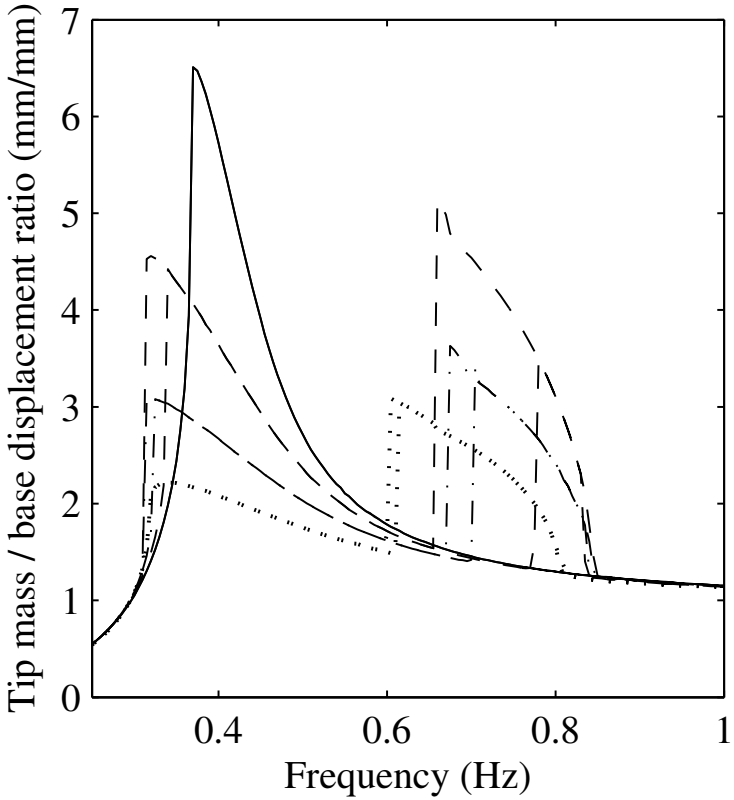

(a) Tip mass response

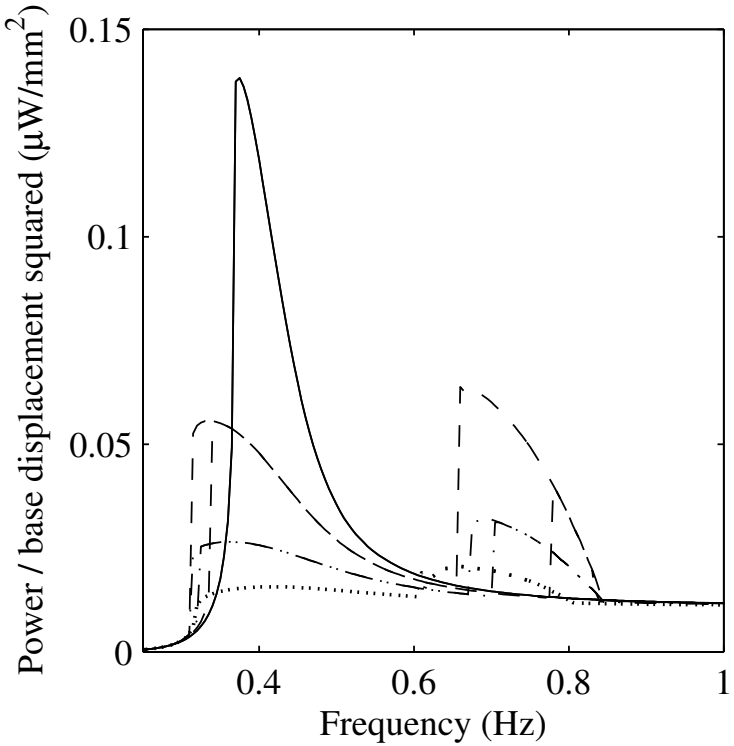

(b) Average harvested power

Figure: The simulated results for a tip mass of $M_t = 14$g, and a base excitation with amplitudes of $z_0 = 5$ (solid), 10 (dashed), 15 (dash-dot) and 20 mm (dotted) at a range of frequencies. $R_l = 9.944\,\mathrm{M}\Omega$ for all cases.

Summary

- The proposed energy harvesting system addresses a very difficult problem where energy is required from a structure with low excitation frequency and high displacement, such as a highway bridge.
- A resonant linear harvester based on a cantilever beam is difficult to implement because the low natural frequency requires a very large or a very flexible beam.
- A low frequency piezoelectric energy harvester is proposed using an inverted elastic beam-mass system.
- The equations of motion for the proposed system were developed, the response was simulated, and this model was validated experimentally.

Summary

- The results show that the harvester has the potential to scavenge power depending on the proper choice of the tip mass and other parameters. In particular, choosing a tip mass so that the beam is almost buckled gives a relative bandwidth (defined using the half power points) up to twice that of the linear harvester.
- The maximum power harvested is also significantly greater, once the lower excitation frequencies are accounted for.
- If the beam is buckled then the system exhibits common nonlinear system characteristics such as co-existing solution, including chaotic responses.
- In the buckled configuration, significant power is only harvested if the excitation is sufficient for the system to hop between the potential wells and hence give a large displacement response.